# 3D printed cathodes for implantable abiotic biofuel cells

M. Ghodhbane, D. Beneventi, A. Zebda, L. Dubois, J.-P. Alcaraz, F. Boucher, J. Boutonnat, G. Menassol, D. Chaussy, N. Belgacem

M. Ghodhbane, D. Beneventi, A. Zebda, L. Dubois, J.-P. Alcaraz, et al.. 3D printed cathodes for implantable abiotic biofuel cells. Journal of Power Sources, 2023, 580, pp.233356. ⟨10.1016/j.jpowsour.2023.233356⟩. ⟨hal-04294558⟩

HAL Id: hal-04294558
https://hal.science/hal-04294558v1

Submitted on 20 Nov 2023

# 3D Printed cathodes for implantable abiotic biofuel cells

M.Ghodhbane[1,2], D. Beneventi[1], A. Zebda[2], L. Du bois[3], J.-P. Alcaraz[2], F. Boucher[2] , J. Boutonnat[4], D. Chaussy[1], N. Belgacem[1]

[1] *Univ. Grenoble Alpes, CNRS, Grenoble INP*, LGP2, 38000 Grenoble, France. *Institute of Engineering Univ. Grenoble Alpes*

[2] *Univ. Grenoble Alpes, CNRS, UMR 5525, VetAgro Sup, Grenoble INP, INSERM, TIMC, 38000 Grenoble, France.*

[3] *Univ. Grenoble Alpes, CEA, CNRS, INAC, SyMMES, Grenoble, 38000, France.*

[4] *Department of Anatomopathology and Cytology, University Hospital, Grenoble, 38000, France.*

## Abstract

3D printing has recently triggered huge attention in several fields such as construction, artificial tissue engineering, food fabrication, wearable electronics, and electrochemical energy storage.
This work investigates the fabrication of a 3D-printed abiotic cathode for implantable glucose/oxygen biofuel cells. The ink formulation was optimized to get printable ink with high electro-catalytic activity. Electrode macro porosity was screened in order to identify the better compromise between electrode density and electrochemical performance. A maximum current density of 260 µA/cm$^2$ was obtained with cylindrical electrodes with linear mesh infill and a volumic infill rate of 40%.
A complete biofuel cell was assembled using a 3D-printed abiotic cathode and an enzymatic anode in the form of a compressed pellet showing maximum power and current densities of 80 µW/cm$^2$ and 320 µA/cm$^2$, respectively. Moreover, the hybrid biofuel cell was implanted in the intraabdominal region of a rat for three months and after cell explantation, the abiotic cathode displayed a 50% decrease in the current density while the enzymatic anode did not display any residual activity.
The 3D printed electrode displayed a 2-3.6 fold increase in current density when compared to homolog 2D electrodes.

## Graphical Abstract

*Implantation of the biofuel cell in a free-living rat for 1 to 3 months*

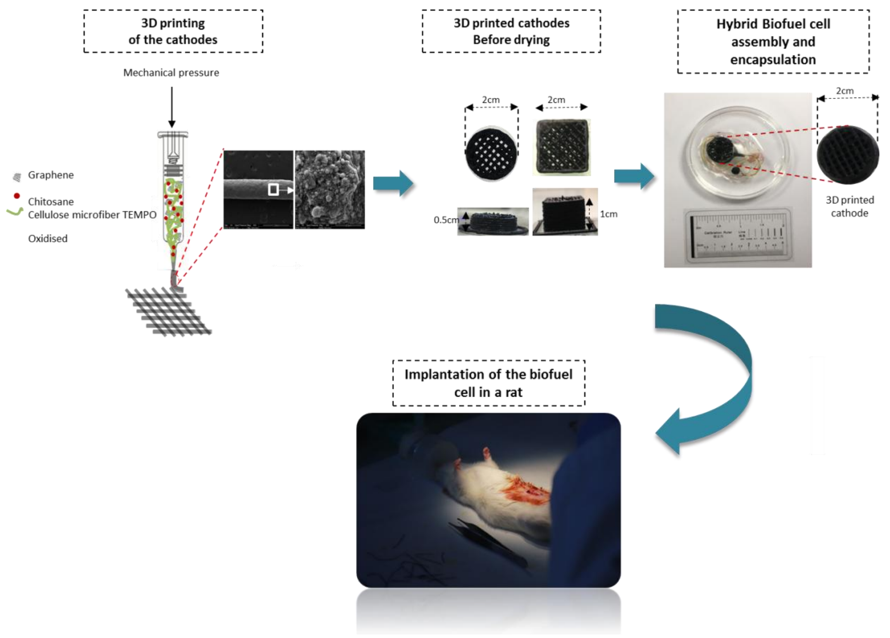

## 1. Introduction

Glucose/$O_2$ biofuel cells (GBFC) have triggered increasing attention due to their unique ability to convert to convert chemical energy stored in human body to electrical energy. The energy conversion is obtained through the anodic oxidation of glucose and the cathodic reduction of oxygen. The continuous presence of oxygen and glucose in the fluidic tissue promotes a theoretically unlimited lifetime. Thus, GBFCs may be a good alternative to lithium-ion batteries.

GBFC could be classified according to the catalyst type: enzymatic, abiotic, and hybrid biofuel cells: i) enzymatic biofuel cells are selective and powerful however they suffer from a limited lifetime due to the progressive enzyme denaturation with time, ii) abiotic biofuel cells are more stable and more biocompatible, iii) hybrid biofuel cells, use both enzymatic and abiotic catalysts. GBFC's can be used as an energy source to power-miniaturized and implantable devices and, since the implantation of the first enzymatic biofuel cell in a rat by *Cinquin et al* in 2010 [1], several research works, aiming at the GBFC implementation, were conducted [1]–[7]. GBFC has been successfully implanted in snails [8], lobsters [9], rats [1], [5] and even a human ex-vivo test has been carried out by *Pankratov et al* [10]. Different GBFC's designs have been tested: flexible GBFC on bucky papers [11], [12], screen printed GBFCs [13]–[15], spray-coated GBFCs [16]…) to 3D bulky pellets realized by compression [2], [5], [17]. However, despite the ease of manufacturing, 3D bulky pellets-based electrodes suffer from limited porosity and electrolyte diffusion. In fact, the electrode's catalytic activity is limited by its compactness and high density which limits the electrolyte accessibility and diffusion within the electrode.

The use of 3D printing can overcome this limitation through the control of the electrode's macro porosity. Thus, better access to the catalytic sites is obtained through the macropores. 3D printing, initially introduced by Charles Hall in 1986, consists of manufacturing three-dimensional objects via a successive deposition of material layers until obtaining the final structure. There are several 3D printing technologies, however, in this work, we will focus on 3D printing by extrusion of concentrated suspensions (LDM or Liquid Deposition Modeling). LDM printers consist of two main components: the printer, which controls the movement and position of the nozzle, and the extruder, which controls the material flow. Three common types of extrusion systems exist, i.e. extrusion via i) a piston driven by a stepper motor, ii) a pneumatic system, or iii) an auger pump. This technique has received great attention during recent years in different fields such as construction [18], energy storage systems [19]–[23], artificial tissue engineering [24]–[26], and food manufacturing [27]–[29]. The use of 3D printing in the field of energy storage allows for obtaining more complex 3D architectures and highly porous electrodes. Recently, this method has been used for the fabrication of lithium-ion batteries [19], [30]-[32], supercapacitors [23], [33]-[35], and glucose biosensors [36]. Different materials have been used. For most of them carbon (i.e. carbon nanotubes [37], reduced graphene oxide [20], carbon [33], etc.) has been combined with a polymer playing the role of both rheology modifier and binder such as cellulose nanofibrils [30], Pluronic® F127 [32], hydroxypropyl methylcellulose [38] and silica gel [36]. Different manufacturing methods have been adopted varying from simple methods, characterized by ink manufacturing then 3D printing [19], [31], [35], and methods requiring additional steps after printing such as chemical or thermal reduction [38], [22], lyophilization [22], [39], [40], electrodeposition [32], [38]. Despite the progress made to introduce additive manufacturing in the field of energy storage/generation devices, the fabrication of 3D-printed electrodes for implantable glucose biofuel cells was not yet explored. In the present work, we use, for the first time, the additive manufacturing process in order to fabricate 3D-printed electrodes with controlled macroporosity for implantable glucose biofuel cells. This study's first step consists of optimizing the gel formulation in order to obtain a 3D printable ink where the rheological modifiers don't affect the catalytic activity. Thereafter, biocathodes were tested *in vitro* and implanted in rats to evaluate their electrochemical performances after different implantation periods and their biocompatibility.

## 2. Experimental Part

### *2.1 Materials*

Low molecular weight chitosan and genipin were purchased from Sigma Aldrich, graphene nanoplatelet aggregates (06-0235) from Strem Chemicals and TEMPO-oxidized Microfibrillated Cellulose (T-MFC) was supplied by CTP (Centre Technique du Papier, Grenoble) [41]. T-MFC were produced from bleached and TEMPO (2,2,6,6-tetramethylpiperidine-1-oxyl radical) oxidated hardwood fibres. A mechanical treatment composed by a sequence of refining and high pressure homogenization (2 passes at 1500 bars) was applied to cellulose fibres to get a gel-like suspension with an T-MFC concentration of 2% w/w. Iron (2%)/Nitrogen doped graphene was fabricated by oxidized graphene nanoplatelets/Iron precursor heat treatment under ammoniac flux as was described in previous works [42],[43].

Multiwalled carbon nanotubes, 1,4 naphtoquinone and glucose deshydrogenase (GDH) used to prepare enzymatic bioanodes were supplied by NanoCyl and Aldrich, respectively.

### *2.2 3D printable hydrogel's formulation*

The hydrogel was prepared by mixing 0.2 g of chitosan, 1 mg of genipin crosslinker and 15 g of T-MFC (2%) with different amounts of doped and not doped graphene. For better homogenization and to prevent nozzle clogging during 3D printing, the prepared ink was processed on a three-rolls mill until getting a hydrogel with a shiny aspect. Four samples were prepared with different total graphene mass percentages (0%, 75%, 80%, and 83% as calculated with respect to the dry materials). The samples composition is given in Table 1. Hydrogels were stored in a refrigerator at 6°C and heated at room temperature before use.

**Table 1.** *Composition of the different prepared formulations expressed as total dry solids content in the aqueous paste and weight fractions of the dry solids. Owing to the extremely low mass used for electrodes formulation, genipin was omitted.*

| Sample | Dry solids content (%) | Chitosan (%) | T-MFC (%) | Graphene (%) |
|---|---|---|---|---|
| $S_1$ | 3.3 | 40 | 60 | 0 % |
| $S_2$ | 12 | 10 | 15 | 75 (1/3 Nitrogen, Iron (2%) doped graphene) |
| $S_3$ | 14.5 | 8 | 12 | 80 (1/4 Nitrogen, Iron (2 %) doped graphene) |
| $S_4$ | 16.9 | 6.6 | 10 | 83.3 (1/5 Nitrogen, Iron (2 %) doped graphene) |

### *2.3 Electrode's 3D printing*

Cathodes were printed using an LDM 3D printer (3D Culture) equipped with a piston extrusion system. To optimize the ink formulation, the four prepared samples were used to print 2×2×1 cm 3D electrodes. The prepared hydrogels were extruded at room temperature using a nozzle of 0.96 mm diameter and a speed of 5 mm/s. The layer height was set to 0.6 mm. The printed cathodes were air dried at room temperature. Using the best formulation, different cathodes shapes were printed such as cuboids and cylinders. The cyclindrical shape with height of 0.25 and 0.5 cm was used to produce electrodes for implantation.

### *2.4 Ink and 3D printed cathodes characterization*

*Rheological properties.* The prepared hydrogels' rheological properties were evaluated with a MCR 301 rheometer (Anton Paar) using a parallel plate with 25 mm diameter and a rotor to stator gap of 1 mm. In order to avoid water evaporation during measurements, a cover was used and the temperature was set to

25°C. Hydrogels viscosities were evaluated as a function of the shear rate and the Herschel Bulkley law was used to fit experimental data and estimate the yield stress and power-law constants, i.e.:

$$\sigma = \tau_0 \dot{\gamma}^{-1} + k\,\dot{\gamma}^{n-1} \qquad (1)$$

where: $\dot{\gamma}$ is the shear rate, $\sigma$ is the viscosity, $\tau_0$ is the yield stress $k$ and $n$ are the power-law constants.

The thixotropic behavior of the composite gels was also explored by a serie of 3 shear rate cycles made of 100 s at a shear rate of 1000 $s^{-1}$ and 100 s at a shear rate of 0.1 $s^{-1}$. All samples were pre-sheared for 100 s at 0.1 $s^{-1}$ before each test. Oscillatory tests were done in order to determine the viscoelastic characteristics of all the prepared hydrogels. The linear viscoelastic region (LVR) was determined by amplitude sweep tests carried out at a frequency of 1 Hz and shear stress varying from 1 to 1000 Pa. The frequency sweep was performed at 0.1% strain from 0.1 to 10 Hz. The evolution of the storage modulus (G'), loss modulus (G"), complex modulus (G*) and loss angle tangent (tan δ = G"/G') were evaluated as a function of frequency. The analyses were conducted in triplicate at 25°C.

*Morphological investigation.* The morphological properties of the 3D printed electrodes were determined using scanning electron microscopy (FEI-Quanta 2000, ESEMTM) equipped with EDX Unit device (Energy Dispersive-ray Analyses). 3D-printed cubes images were realized with optical microscopy. These images were treated by the software Image J to evaluate mesh pore's distribution. Owing to the pore square shape generated by 3D printing, pore shape was expressed as equivalent square size.

*Specific surface area measurement.* Nitrogen adsorption-desorption isotherms were measured on a surface area analyzer NOVAtouch™ 2 (Quantachrome Instruments) at 77 K. Before the measurements all samples were degassed under vacuum at 40°C for 12 h. Based on the obtained data, samples' specific surface areas were calculated using the Brunauer–Emmett–Teller (BET) linear equation in the approximate relative pressure range from 0.1 to 0.3. The correlation coefficient of the linear regression was not less than 0.999. The total pore volume was calculated from the volume adsorbed at $p/p_0$~0.99.

### *2.5 Bioanodes fabrication.*

The bioanode was fabricated according to procedures described in our previous study [44]. The FQDGDH enzyme was selected since it does not use oxygen as electron acceptor without competing with the cathode [45]. Pellets of 0.5 $cm^2$ diameter, and 0.3 cm thickness) were fabricated by the hydraulic compression of a mixture of MWCNTs-NQ (10 mg) were the MWCNTs were obtained by mixing and then drying under vacuum a ratio of 1:1 MWCNTs/naphtoquinone in 3ml of acetonitrile. In order to set up the electrical connection, a copper wire was embedded in the carbon paste covering one side of the disc. The perimeter and the covered side of the disc were isolated with silicone. The resulting bioanode was dried at ambient temperature for 12 h and then stored at 4 °C until use in PBS buffer solution.

### *2.6 Electrochemical properties.*

The electrochemical characterizations were performed using a three-electrode electrochemical cell associated with a Biologic Potentiostat SP150. The 3D printed biocathode was glued to a conductive teflonated gas diffusion layer and used as a working electrode, a platinum electrode was used as a counter electrode and a saturated calomel electrode (SCE) as a reference electrode.

The 3D printed abiotic biocathodes were tested at ambient temperature (20 ± 3°C) in a pH 7.4 physiological medium, i.e. 100 mL of a solution containing phosphate buffer (0.01 mol $L^{-1}$), NaCl (0.14 mol $L^{-1}$), KCl (0.0027 mol $L^{-1}$). The chronoamperometric response of the biocathode was recorded at 0.1 V vs. SCE for 24h under air and saturated oxygen. A complete biofuel cell was assembled using the FAD-GDH based enzymatic anode (0.5 cm diameter and 0.2 mm thickness) and a 3D printed cylindrical abiotic cathode (1.5 cm diameter, 2.5 mm thickness). Anodes were characterized by linear sweep voltammetry at 2 mV/s between 0 mV Vs. OCP and 0.05 Vs. SCE.

### *2.7 Biofuel cell Implantation*

A 3D printed cylindrical cathode with a diameter of 1.5 cm was prepared for the implantation step. This cathode was assembled with an FAD-GDH based enzymatic anode. The two electrodes were connected to a resistance of 80 kOhm. As illustrated in Fig. 1 the hybrid biofuel cell was protected by a PVA membrane with a sandwich-like design. The surrounding PVA acts as a biocompatible and porous interface between the biofuel cell and the body [44]. This setup was dried overnight then sterilized using gamma radiation (60Co source). The cathode was finally implanted for one or three months in the abdominal cavity of a male wistar rat before autopsy and cell explantation and analysis. Details dealing with surgical and postoperative procedures followed during cell implantation and explantation are described in a previous work [46].

### 2.8 Ethical protocols

Experiments were conducted in accordance with the Directive L276-33 2010/63/EU on the protection of animals used for scientific purposes and the recommendations from the Declaration of Helsinki. The protocol has been validated by the Ethics Committee (#12) of Grenoble Alpes University and approved by the French Minister of Research (agreement: APAFIS# 2018042409479645).

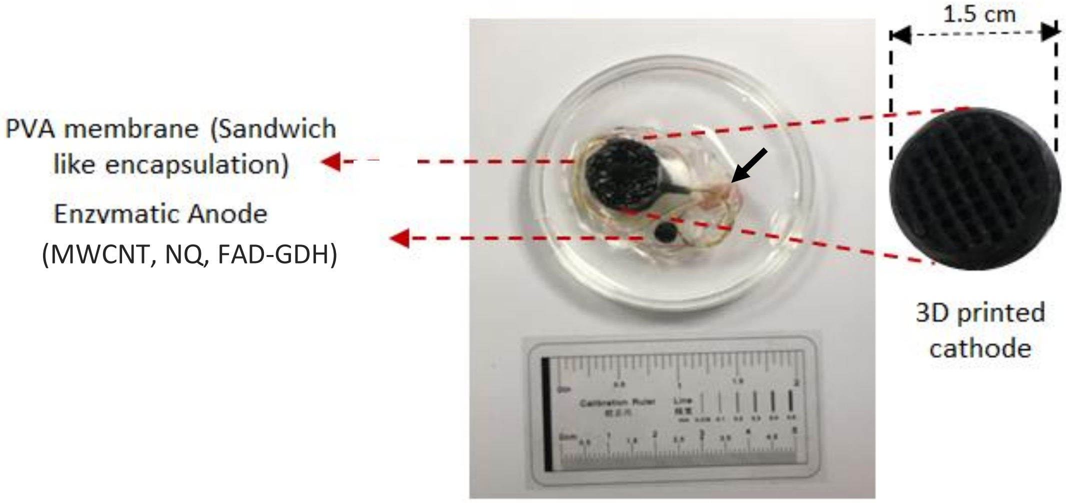

**Fig. 1.** *Hybrid biofuel cell assembly and encapsulation for the implantation step. The black arrow shows the 80 kOhm resistance.*

## 3 Results and discussion

### 3.1 Rheological tests

Hydrogels viscosity was measured as a function of the shear rate and experimental data shown in Fig. 2a display a shear-thinning behavior for all tested hydrogels, as expected from the typical orientation along the shear direction of dissolved macromolecules and suspended fibres/particles when increasing in the shear rate. The lowest viscosity was measured with the formulation S1 consisting of chitosan and T-MFC. The addition of graphene nanoplatelets induced a progressive increase in viscosity from 40 to 200 Pa.s at a shear rate of 1 $s^{-1}$ and of the shear thinning behavior, as indicated by power-law coefficients *k* and *n* (Table 2). Moreover, the progressive increase of the yield stress ($\tau_0$) from 40 to 215 Pa.s at increasing graphene concentration, highlights the role of graphene platelets in preventing viscous flow. The 3D printability and shape fidelity of the prepared hydrogels was characterized by exploring their thixotropic properties and their recovery rate. Those properties were investigated by applying a high shear rate of 1000 $s^{-1}$ which was suddenly decreased to 0.1 $s^{-1}$. This is a simulation of what happens during the 3D printing: the high shear rate is assimilated to the ink flow through the nozzle, whereas the low shear rate corresponds to the hydrogel final state once printed. The recovery rate represents the ability of the ink to recover its structure and high viscosity after intense shear. It is expressed in percentage and calculated from the difference between the viscosity after the initial pre-shearing at 0.1 s$^{-1}$ and after each shearing cycle.

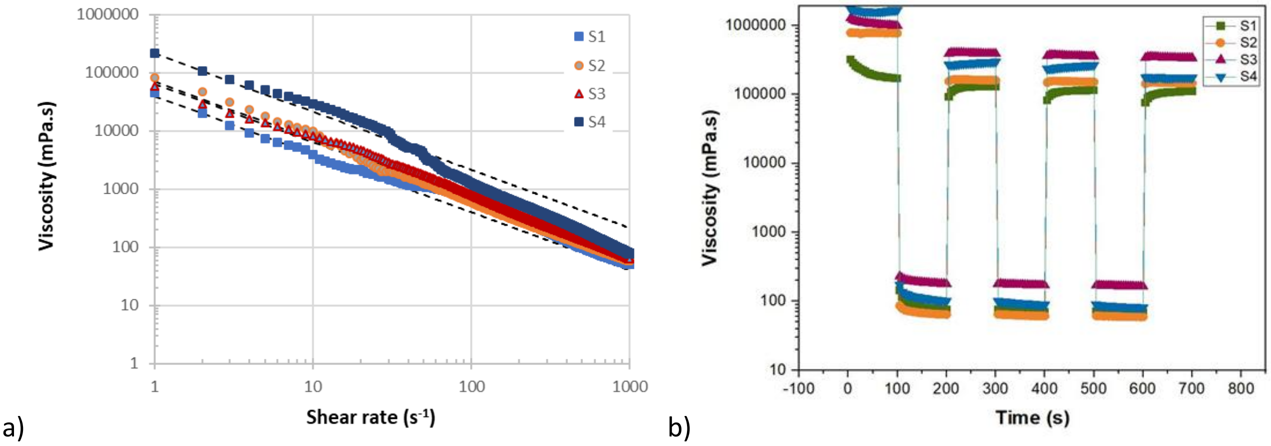

**Fig. 2.** *a) Viscosity of MFC/chitosan/graphene hydrogels plotted as a function of the shear rate (dotted lines represent data interpolation with the Herschel-Bulkley law), b) the thixotropic behaviour of the different samples.*

**Table 2.** *Rheological properties of tested aqueous suspensions. Herschel-Bulkley law parameters ($\tau_0$, n, k) recovery rate, critical shear stress and height as obtained from rheograms and eq. 2.*

| **Sample** | **$\tau_0$ (Pa.s)** | **n** | **k (m Pa.s$^n$)** | **Recovery rate (%)** | **Critical Shear stress $\tau_f$ (Pa)** | **Critical height (cm)** | **Photos of printed cubes (2 cm side)** |
|---|---|---|---|---|---|---|---|
| **$S_1$** | 40 | 0.26 | 55 | 2.8 | 28.6 | 0.41 | 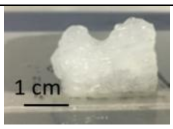 |
| **$S_2$** | 65 | 0.10 | 50 | 10.5 | 84 | 1.21 | 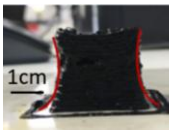 |
| **$S_3$** | 71 | 0.06 | 150 | 42 | 109 | 1.57 | 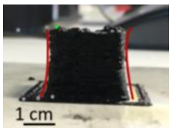 |
| **$S_4$** | 215 | 0.09 | 150 | 45.2 | 343 | 4.94 | 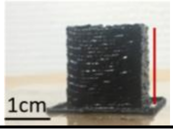 |

Fig. 2b and data in Table 2 show that the best recovery rate was given by the sample with the highest graphene content. It is therefore possible to argue that at low shear rate graphene particles interaction lead to an increased yield stress and a high viscosity which decrases with the progressive particles orientation as the shear rate is increased.

Viscosity recovery as the shear rate abruptly decreases (Fig. 2b) clearly shows that, even at high graphene concentration, the aqueous suspension quickly recovers its unsheared structure, high viscosity and yield stress. Rotational tests show that within the range of tested concentration, adding graphene helps to improve the 3D printability. For higher graphene fractions extrusion problems were observed thereafter the maximum graphene mass fraction was kept equal to 83.3%.

Fig. 3a shows the curves of the elastic (G') and viscous (G") modulus plotted as a function of the shear stress for all the prepared samples. The critical strain and the LVER determined from these curves shows that graphene addition induces a progressive increase of the critical shear stress from 29 to 343 Pa.s (Fig. 3a and

Table 2) which is in line with the yield stress increase evaluated using Equation 1. The largest LVER region and the highest critical shear stress value were obtained with the highest graphene mass fraction (S4) thus confirming that graphene improves the gel microstructure.

Sweep frequency tests (Fig. 3b) show that when increasing the graphene fraction, the elastic modulus G' increases and G'> G'', which means that the gel strength is increasing with the graphene concentration and that all the samples are well structured. Moreover, G' and G" are frequency-independent which indicates that all the prepared samples have a gel-like behavior.

Moreover, all samples displayed a loss factor <1 which means that the hydrogel has a stable solid-like structure (Fig 3b).

In order to evaluate the static stability of 3D printed objects, the critical height, $H_{cr}$, before the onset of viscous deformation of the base layer was calculated as [47]:

$$H_{cr} = \frac{\tau_f\sqrt{3}}{\rho g} \qquad (2)$$

where $\rho$ is the hydrogel density, $g$ is the gravitational constant and $\tau_f$ is the critical shear stress.

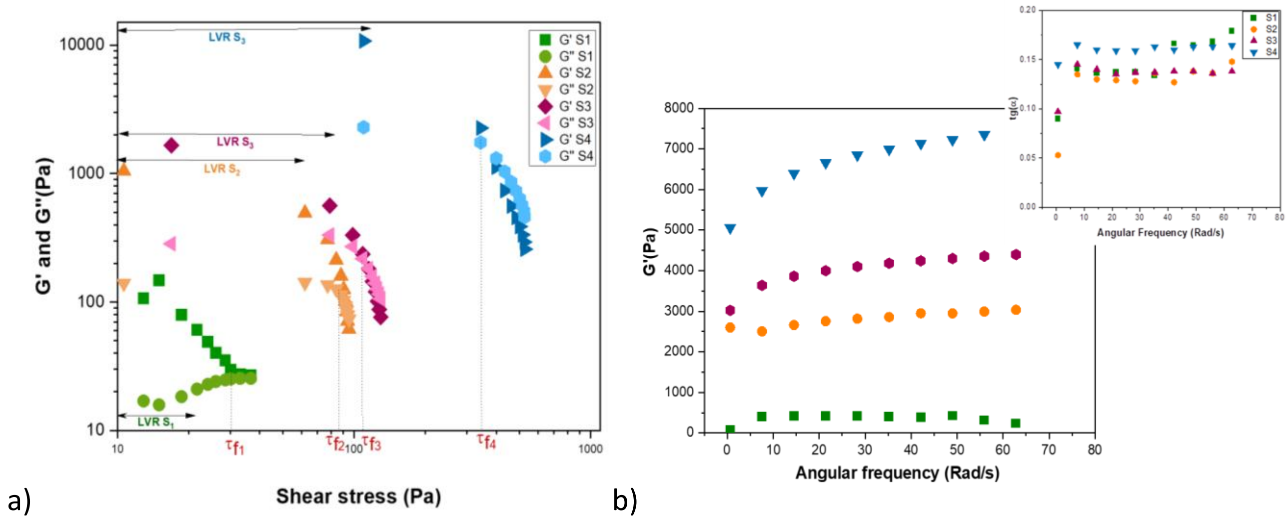
a)

b)

**Fig. 3.** a) *Elastic and viscous modulus plotted as a function of the shear stress of the prepared samples ($S_1$, $S_2$, $S_3$, $S_4$) at a frequency of 1 Hz. b) Elastic modulus and loss angle's tangent (inset) plotted as a function of the angular frequency.*

The comparison between the shape of 3D printed bulky cubes and the critical-shear stress, -height of the corresponding hydrogel formulation (Table 2) shows that there is no shape fidelity for the T-CMF-Chitosan hydrogels with graphene content lower than 80% ($S_1$-$S_3$ samples). Whereas, with a graphene content of 83.3% ($S_4$) the shape fidelity is preserved, which is in line with the rheological behavior of tested hydrogels. Owing to a better printability and a high graphene content, only the hydrogel formulation $S_4$ will be used to 3D print cathodes.

### *3.2 Electrode 3D printing, infill optimization*

The theoretical volumic infill (linear grid pattern) and the macroporosity of 3D printed electrodes was varied between 25 and 100% and corresponding samples were labeled as $S_{25\%}$-$S_{100\%}$. Table 5 shows that all the 3D-printed cuboids, were subjected to deformation with retractions varying between 40-48% and 29-33% in height and length, respectively. This deformation is more pronounced with low infill rates, and it can be associated to a limited number of contact points and unsupported filament segments in the infill mesh. Image analysis of macropores generated on the XY plane during 3D printing with different nominal infill ratios (Fig. 4a) shows that the equivalent pore size progressively decreases from ca. 1.5 to 0.3 mm when the infill ratio rises from 25 to 50%. Moreover, the irregular width of the deposed filament and print defects, as shown in Fig. 4a, generate a not negligible scattering in the pore size distribution and pores clogging at high infill rate where the detected macropores number drops when the infill rate increases from 40 to 50%. In parallel to the generation of a dense mesh structure, the increase of the infill ratio leads to a different distribution of the electrode material, indeed the 3D electrodes are composed by bulky perimeter shells, i.e. a stack of 1 mm width filaments, and an internal mesh made by 0.6 mm diameter filaments. The calculation of the electrode material volume fraction in the mesh structure (inset in Fig. 4a) shows that the increase of the infill rate leads to a relative increase of the electrode material in the mesh structure which rises from 48 to 60% when the infill ratio is increased from 25 to 40%, i.e. before clogging of the 3D printed mesh. SEM analysis of electrode sections (Fig. 4) shows that pores in the ZX and ZY planes generated by layer stacking had an irregular thickness ranging between 0.1 and 0.4 mm which was associated with filament deformation when deposed on unsupported areas.

Specific surface area measurements through nitrogen adsorption-desorption ($S_{BET}$) on 3D printed cubes summarized in Table 3, show that at low infill rates (<50%) electrodes SSA has a nearly constant value of 560 $m^2/g$, whereas for higher infill rate it slightly decreases to 535 $m^2/g$. This trend was interpreted as reflecting lower pores accessibility in high infill rate and bulk electrodes.

The specific surface area (SSA) of the formulation $S_4$ calculated using its composition and the SSA of each component in powder (i.e. 750 $m^2/g$, 300-400 $m^2/g$ and 1-7 $m^2/g$, for graphene nanoplatelets, cellulose nanofibers [48] and chitosan [49], respectively) ranged between 650 and 662 $m^2/g$ thus indicating that materials blending and 3D printing in the form of macroporous electrode leads to a 16% decrease in SSA. Since SEM analysis of electrode/filament highlighted the presence of fissures in both filament surface and internal structure (Fig. 4b and c), the slight decrease in SSA was associated with the presence of open pores in both 3D electrodes and unit filaments. Overall, it can be concluded that all tested 3D electrodes have high prorosity, nevertheless if the microporosity is nearly constant (as shown by SSA measurements), surface macroporosity generated by 3D printed patterns, sharply decreases for infill ratios higher than 40%.

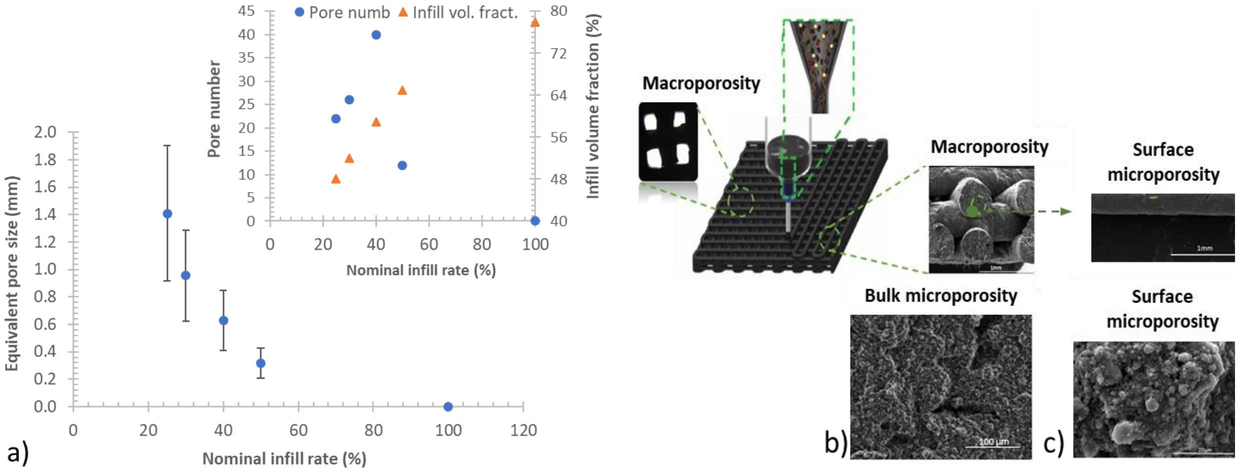

**Fig. 4.** *a) Effect of the nominal infill during 3D printing on the size of macropores. Inset shows the pore number and the theoretical electrode material volume fraction in the infill mesh plotted as a function of the infill rate. SEM pictures of* a) section of a 3D electrode on the ZY plane and b) surface of a dried unit filament.

***Table 3.*** *Effect of the nominal infill rate on the specific surface area, shape and specific current in air and oxygen (100 mV Vs. SCE in PBS neutral media) of 3D printed cuboid cathodes.*

| Sample | Nominal infill rate (%) | Specific surface area ($m^2/g$) | Specific current in air (µA/mg) | Specific current in $O_2$ (µA/mg) | 3D cathodes with varying infill rate |
|---|---|---|---|---|---|
| $S_{25\%}$ | 25 | 558 ±5 | 2.1 | 8.3 | 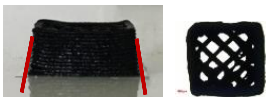 |
| $S_{30\%}$ | 30 | 574 ±2 | 3.8 | 8.8 | 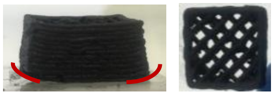 |
| $S_{40\%}$ | 40 | 560 ±2 | 8 | 13.2 |  |
| $S_{50\%}$ | 50 | 552 ±4 | 3.9 | 9.6 |  |
| $S_{100\%}$ | 100 | 535 ±2 | 2.5 | 6.2 |  |

### 3.3 Effect of electrode structure on the electrochemical performance

Due to the significant capacitive current produced by the high volume of the 3D-printed abiotic cathodes, it becomes challenging to accurately detect the electrocatalytic response within the cyclic voltammetry (CV) curve. As a result, chronoamperometry measurement was selected as the preferred method for investigating the cathode's electrochemical performance. The chronoamperometry tests were performed at room temperature, pH 7.4, and a potential of 100 mV (Table 3). The results revealed that the oxygen reduction current progressively increased with the saturation of the solution with oxygen, indicating the catalytic activity of the cathode towards oxygen reduction. These findings are consistent with our prior research on the ability of Iron/Nitrogen doped graphene to catalyze $O_2$ reduction under physiological conditions [42], [44].

The catalytic currents (expressed as a function of catalyst mass) of 3D electrodes were affected by the nominal infill rate. Indeed, the catalytic currents, under air and oxygen, progressively increased from 2.3-8.7 µA/mg to 8.1-13 µA/mg when the infill rate was increased from 25 to 40%, respectively corresponding to a maximum current density per surface of 400 µA/$cm^2$ under air and 700 µA/$cm^2$ under oxygen. Above 40% infill, the current density decayed to 3.9-9.5 µA/mg and 2.8-6.2 µA/mg for infills of 50 and 100%, respectively. The presence of a peak in the specific current generated by 3D electrodes with different infill ratio was associated with the electrode structure and the different material distribution. Below 40% infill rate, the progressive increase of the relative amount of electrode material in the porous mesh structure leads to better filament wetting by the electrolyte and an increase of the specific current. Whereas above 40% infill macropores clogging lowers electrolyte penetration into the porous electrode leading to a drop of the specific current. An infill rate of 40% was therefore selected to print cylindrical electrodes for implantation.

The current generated by cylindrical electrodes under air and oxygen (Fig. 5a) was slightly affected by the electrode height and matched with values obtained with the homologous cuboid electrode. Similar current values obtained for electrode heights of 0.25 and 0.5 cm was interpreted as reflecting the complete wetting of the porous electrode by the electrolyte and the absence of occluded macropores when using an infill rate of 40%.

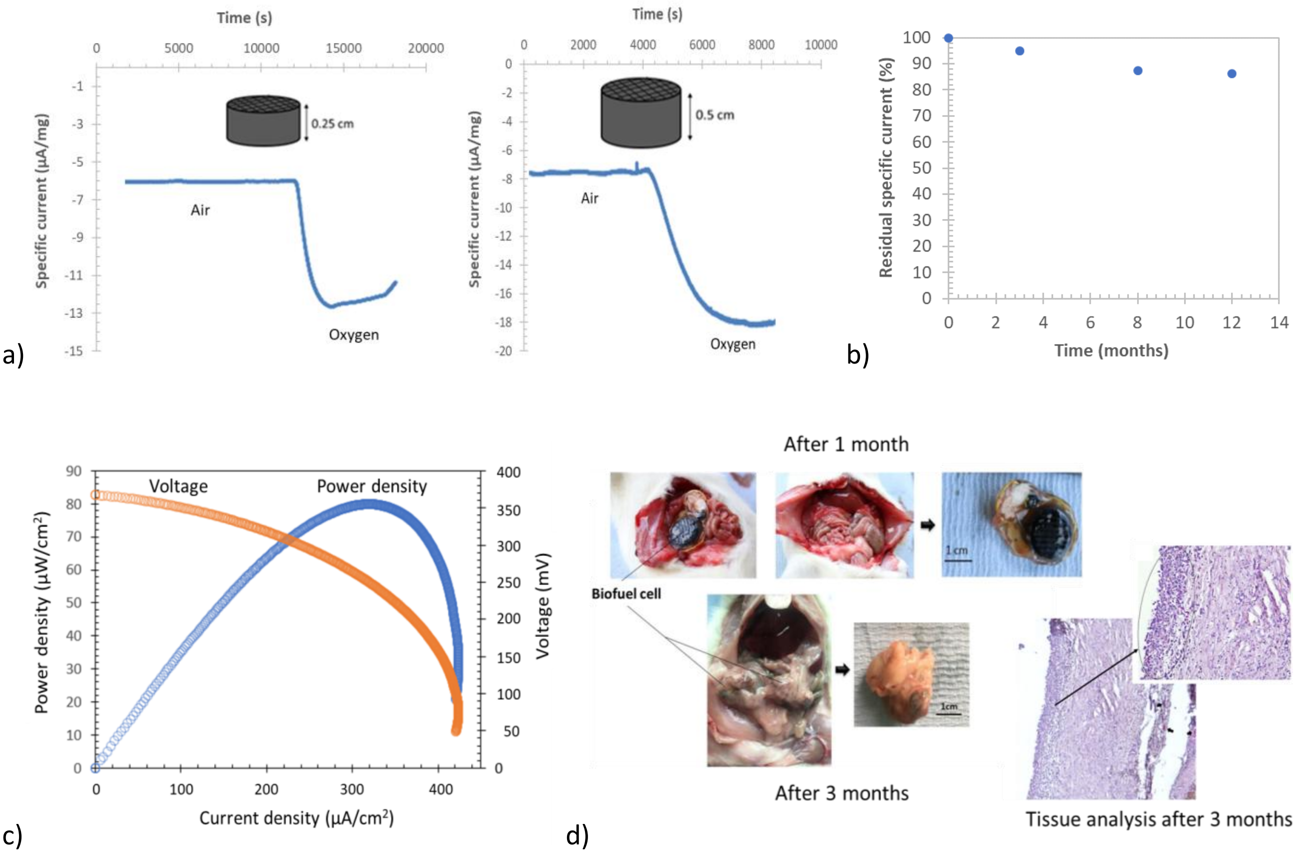

***Fig. 5.*** *Complete biofuel cell assembly and testing. a) Chronoamperometries at 100 mV. Vs. SCE in a physiological medium (pH=7.4) of 3D printed cylindrical electrodes at a filing rate of 40 % biocathodes with a diameter of 1.3 cm and a thickness of 0.25 cm. b) Cathode specific current variation during in vitro electrodes aging. c) Potential vs. current density and polarization curve of the hybrid biofuel cell (3D printed biocathode and bioanode based on FAD-GDH) in a phosphate buffer at pH = 7.4 with 5 mM of glucose before implantation. d) Biofuel cell explanation after 1 and 3 months and x3/x4 microscopy images of tissue surrounding the biofuel cell after 3 months implantation (the dotted circle highlights the zone in contact with the biofuel cell.*

Electrodes with the selected formulation and infill rate displayed a slight decrease of the specific current upon prolonged aging (Fig. 5b) with an average decrease of ca. 1.3%/month with respect to the pristine current. A partial deactivation of catalytic sites or active material release due to microfibrillated cellulose swelling upon a prolonged contact with the electrolyte were supposed to be at the origin of this limited but steady decrease of the electrode performance. Overall, the cylindrical cathode used for the complete biofuel cell assembly had an apparent surface of 1.33 cm$^2$, a thickness of 0.25 cm, an active material content of 38.4 mg, an open circuit potential of 0.36 ± 0.1 mV Vs. SCE (as obtained from 1h records) and a current density of 168 µA/cm$^2$ and 382 µA/cm$^2$ at 100 mV under air and oxygen, respectively.

When compared to homologue 2D biocathodes manufactured by blade-coating [42], 3D cathodes displayed a 2-3.5 fold increase in the current density (i.e. from 5 to 18 µA/mg in $O_2$), and 2 times higher than compact pellet electrodes [44]. This is correlated with the higher porosity and specific surface area of 3D electrodes, i.e., 10-70 to 560 m$^2$/g for the 2D and 3D electrode, respectively.

### *3.4 Enzymatic bioanode and full cell*

FAD-GDH-based enzymatic bioanodes were used to assembly the biofuel cell. After 5 mM glucose injection, the pellet bioanode generated a current attaining a plateau at 250 µA/cm$^2$ at 0 mV Vs. SCE (corresponding to a neat current of 50 µA) after 20 min. The obtained current corresponds to the electrocatalytic oxidation of glucose by FAD-GDH demonstrating the bioelectrode ability to catalyze the glucose oxidation process. The bioanode was subsequently coupled with the cylindrical 3D printed cathode to construct a glucose biofuel cell. In vitro testing of the complete biofuel cell in a physiological buffer at pH 7.4 and a glucose concentration of 5 mM (Fig. 5c) revealed an open circuit voltage of 360 mV and a maximum power density delivery of approximately 80 µW/cm$^2$ at a current density of 320 µA/cm$^2$ and a voltage of 260 mV (see Fig. 5c). Above 350 µA/cm$^2$ mass transport losses became dominant inducing a sharp decrease in power density and limiting the maximum current density to 420 µA/cm$^2$. According to data found in the literature [50], the hybrid biofuel cell developed in this study using a 3D nitrogen-doped cathode delivers maximum power and current density comparable to those of high energy density implantable fuel cells using Pt and Au-based electrodes.

### *3.5 Biofuel cell's Biocompatibility evaluation and electrochemical characterization after implantation*

The monitoring of the behaviour and the weight of the rats during the implantation did not reveal any detrimental impact of the presence of the implants thanks to the biocompatible and permeable PVA casing. After 1- or 2-months implantation, rats were euthanized by lethal injection of pentobarbitone (100 mg/kg body weight). The autopsy did not reveal any alteration of the abdominal organs (Fig. 5d). Biocathodes after 1- and 3-months of implantation are shown in Fig. 5d.

The histological analysis of cellular tissue after 3 months implantation showed the presence of a highly vascularized connective tissue (vessels are pointed by arrows) revealing the presence of inflammatory reactions. Tissues in contact with the implant display moderate histiocytic infiltration accompanied by the presence of endothelial cells. These findings confirm our previous data on gel-like polymer membranes that PVA coating minimizes the fibrous encapsulation of implanted biofuel cells [46].

After removal of the surrounding adipose tissue, the biofuel cell potential was measured, showing values of 180 mV and 250 mV after 1- and 3-months implantation respectively. Biocathodes were subjected to an in vitro electrochemical study in a physiological buffer at pH=7.4. Chronoamperometries performed on unit electrodes after cell disassembly showed that:

i) Bioanodes do not show any residual reactivity towards glucose even at concentrations up to 50 mM. Anodes failure was associated to a possible release of the mediators or enzymes denaturation and deactivation.

ii) Both biocathodes are still able to electro catalyze oxygen, indeed current densities of 55-180 µA/cm$^2$ and 53-140 µA/cm$^2$ were recorded under air-oxygen after 1- and 3-months implantation, respectively.

Current density losses of 52% and 63% (under oxygen) after 1- and 3-months implantation demonstrate that the 3D printed abiotic cathode developed in this study can operate in continuous discharge up to periods exceeding 3 months in the body of a rat.

## 4. Conclusion

In this work, chitosan, nitrogen doped graphene and microfibrillated cellulose have been used for the formulation of hydrogels with rheological properties (i.e yield stress and viscoelastic behaviour) adapted to LDM 3D printing and the production of porous abiotic cathodes.

The current density of 3D printed cathodes was strongly affected by the infill rate used during 3D printing and by the ensuing macroporosity and reached a maximum of 14-18 µA/mg (under oxygen) for a volumic infill rate of 40%. Above 40% infill the progressive pores clogging induced a drop in current density.

3D cathodes with optimized design displayed excellent stability upon in vitro and in vivo aging. Indeed, a current density drop of ca. 14% and 63% was observed after 12 months in vitro- and 3 months in vivo-aging.

Complete biofuel cells made of a 3D abiotic cathode and a FAD-GDH enzyme anode were assembled and implanted in rats. The pristine biofuel cells supplied a power density of 80 µW/cm$^2$ and after 1 month implantation anode failure led to stop operating. Autopsy and tissues analysis after 1- and 3-months implantation in rats, did not reveal the presence of severe inflammatory reactions.

Overall, this work demonstrates that 3D printing can be effectively used to produce porous abiotic cathodes delivering a current density up to 3.6 folds higher than 2D homologues. Moreover, the developed materials formulation displays an excellent resistance to both in vitro and in vivo aging.

**Declaration of competing interest**

The authors declare that they have no known competing financial interests or personal relationships that could have appeared to influence the work reported in this paper.

**Data availability**

Data will be made available on request.

**Acknowledgements**

This work was supported by the National Research Agency, France (Implantable Abiotic Biofuel Cell – IMaBiC, ANR-16-CE19-0007) France, the "Laboratoire d'Excellence" Tec21 France, Region Auvergne Rhône Alpes SCUSI program 2018 (no. 187370) and Pack Amb Int'l 2019 (no. Pack Amb Int'l 2019).

The authors thank L. Cortella for the access to radiation facilities at ARC-Nucléart (CEA Grenoble).

**References**

[1] P. Cinquin *et al.*, A Glucose BioFuel Cell Implanted in Rats, *PLOS ONE*, vol. 5, n° 5, p. e10476, mai 2010, doi: 10.1371/journal.pone.0010476.

[2] S. El Ichi, D. K. Martin, P. Cinquin, A. Zebda, « Implantable Biocompatible Reactor », Patent WO2015145054A2, 1 October 2015. https://patentscope.wipo.int/search/en/detail.jsf?docId=WO2015145054&tab=PCTDESCRIPTION

[3] S. El Ichi-Ribault *et al.*, Remote wireless control of an enzymatic biofuel cell implanted in a rabbit for 2 months, *Electrochimica Acta*, vol. 269, p. 360- 366, 2018, doi: 10.1016/j.electacta.2018.02.156.

[4] K. MacVittie, T. Conlon, et E. Katz, A wireless transmission system powered by an enzyme biofuel cell implanted in an orange, *Bioelectrochemistry*, vol. 106, p. 28- 33, 2015, doi: 10.1016/j.bioelechem.2014.10.005.

[5] A. Zebda *et al.*, Single Glucose Biofuel Cells Implanted in Rats Power Electronic Devices, *Sci Rep*, vol. 3, n° 1, p. 1- 5, 2013, doi: 10.1038/srep01516.

[6] C. Gonzalez-Solino, M. Lorenzo, C. Gonzalez-Solino, et M. D. Lorenzo, Enzymatic Fuel Cells: Towards Self-Powered Implantable and Wearable Diagnostics, *Biosensors*, vol. 8, n° 1, p. 11, 2018, doi: 10.3390/bios8010011.

[7] S. Kerzenmacher, J. Ducrée, R. Zengerle, et F. von Stetten, Energy harvesting by implantable abiotically catalyzed glucose fuel cells, *Journal of Power Sources*, vol. 182, n° 1, p. 1- 17, 2008, doi: 10.1016/j.jpowsour.2008.03.031.

[8] L. Halámková, J. Halámek, V. Bocharova, A. Szczupak, L. Alfonta, et E. Katz, Implanted Biofuel Cell Operating in a Living Snail, *J. Am. Chem. Soc.*, vol. 134, n° 11, p. 5040- 5043, 2012, doi: 10.1021/ja211714w.

[9] K. MacVittie *et al.*, From "cyborg" lobsters to a pacemaker powered by implantable biofuel cells, *Energy Environ. Sci.*, vol. 6, n° 1, p. 81- 86, 2012, doi: 10.1039/C2EE23209J.

[10] D. Pankratov *et al.*, Ex vivo electric power generation in human blood using an enzymatic fuel cell in a vein replica, *RSC Adv.*, vol. 6, n° 74, p. 70215- 70220, 2016, doi: 10.1039/C6RA17122B.

[11] A. J. Gross, M. Holzinger, et S. Cosnier, Buckypaper bioelectrodes: emerging materials for implantable and wearable biofuel cells, *Energy Environ. Sci.*, vol. 11, n° 7, p. 1670- 1687, juill. 2018, doi: 10.1039/C8EE00330K.

[12] L. Hussein *et al.*, Decorated nanotube buckypaper as electrocatalyst for glucose fuel cells, p. 2254- 2257, 2009, doi: 10.1109/sensor.2009.5285597.

[13] M. Albareda-Sirvent, A. Merkoçi, et S. Alegret, Configurations used in the design of screen-printed enzymatic biosensors. A review, *Sensors and Actuators B: Chemical*, vol. 69, n° 1- 2, p. 153- 163, 2000, doi: 10.1016/S0925-4005(00)00536-0.

[14] I. Shitanda, S. Kato, S. Tsujimura, Y. Hoshi, et M. Itagaki, Screen-printed, Paper-based, Array-type, Origami Biofuel Cell, *Chem. Lett.*, vol. 46, n° 5, p. 726‑ 728, 2017, doi: 10.1246/cl.170047.

[15] I. Shitanda, S. Nohara, Y. Hoshi, M. Itagaki, et S. Tsujimura, A screen-printed circular-type paper-based glucose/O2 biofuel cell, *Journal of Power Sources*, vol. 360, p. 516‑ 519, 2017, doi: 10.1016/j.jpowsour.2017.06.043.

[16] A. Ben Tahar *et al.*, Carbon nanotube-based flexible biocathode for enzymatic biofuel cells by spray coating, *Journal of Power Sources*, vol. 408, p. 1‑ 6, 2018, doi: 10.1016/j.jpowsour.2018.10.059.

[17] A. Zebda, C. Gondran, A. Le Goff, M. Holzinger, P. Cinquin, et S. Cosnier, Mediatorless high-power glucose biofuel cells based on compressed carbon nanotube-enzyme electrodes, *Nature Communications*, vol. 2, n° 1, Art. n° 1, 2011, doi: 10.1038/ncomms1365.

[18] C. Buchanan et L. Gardner, Metal 3D printing in construction: A review of methods, research, applications, opportunities and challenges, *Engineering Structures*, vol. 180, p. 332‑ 348, 2019, doi: 10.1016/j.engstruct.2018.11.045.

[19] Y. Bao, Y. Liu, Y. Kuang, D. Fang, et T. Li, 3D-printed highly deformable electrodes for flexible lithium ion batteries, *Energy Storage Materials*, vol. 33, p. 55‑ 61, déc. 2020, doi: 10.1016/j.ensm.2020.07.010.

[20] C. W. Foster *et al.*, 3D Printed Graphene Based Energy Storage Devices, *Scientific Reports*, vol. 7, n° 1, Art. n° 1, 2017, doi: 10.1038/srep42233.

[21] U. Gulzar, C. Glynn, et C. O'Dwyer, Additive manufacturing for energy storage: Methods, designs and material selection for customizable 3D printed batteries and supercapacitors, *Current Opinion in Electrochemistry*, vol. 20, p. 46‑ 53, 2020, doi: 10.1016/j.coelec.2020.02.009.

[22] J. Zhang *et al.*, 3D-printed functional electrodes towards Zn-Air batteries, *Materials Today Energy*, vol. 16, p. 100407, juin 2020, doi: 10.1016/j.mtener.2020.100407.

[23] K. Shen, J. Ding, et S. Yang, 3D Printing Quasi-Solid-State Asymmetric Micro-Supercapacitors with Ultrahigh Areal Energy Density, *Advanced Energy Materials*, vol. 8, n° 20, p. 1800408, 2018, doi: 10.1002/aenm.201800408.

[24] R. E. Abouzeid, R. Khiari, D. Beneventi, et A. Dufresne, Biomimetic Mineralization of Three-Dimensional Printed Alginate/TEMPO-Oxidized Cellulose Nanofibril Scaffolds for Bone Tissue Engineering, *Biomacromolecules*, vol. 19, n° 11, p. 4442‑ 4452, 2018, doi: 10.1021/acs.biomac.8b01325.

[25] S. F. S. Shirazi *et al.*, A review on powder-based additive manufacturing for tissue engineering: selective laser sintering and inkjet 3D printing, *Sci. Technol. Adv. Mater.*, vol. 16, n° 3, p. 033502, 2015, doi: 10.1088/1468-6996/16/3/033502.

[26] R. Attalla, C. Ling, et P. Selvaganapathy, Fabrication and characterization of gels with integrated channels using 3D printing with microfluidic nozzle for tissue engineering applications, *Biomed Microdevices*, vol. 18, n° 1, p. 17, 2016, doi: 10.1007/s10544-016-0042-6.

[27] F. C. Godoi, S. Prakash, et B. R. Bhandari, 3D printing technologies applied for food design: Status and prospects, *Journal of Food Engineering*, vol. 179, p. 44‑ 54, 2016, doi: 10.1016/j.jfoodeng.2016.01.025.

[28] J. Sun, W. Zhou, L. Yan, D. Huang, et L. Lin, Extrusion-based food printing for digitalized food design and nutrition control, *Journal of Food Engineering*, vol. 220, p. 1‑ 11, 2018, doi: 10.1016/j.jfoodeng.2017.02.028.

[29] J. Sun, Z. Peng, W. Zhou, J. Y. H. Fuh, G. S. Hong, et A. Chiu, A Review on 3D Printing for Customized Food Fabrication, *Procedia Manufacturing*, vol. 1, p. 308‑ 319, 2015, doi: 10.1016/j.promfg.2015.09.057.

[30] D. Cao *et al.*, 3D Printed High-Performance Lithium Metal Microbatteries Enabled by Nanocellulose, *Advanced Materials*, vol. 31, n° 14, p. 1807313, 2019, doi: 10.1002/adma.201807313.

[31] J. Li, M. C. Leu, R. Panat, et J. Park, A hybrid three-dimensionally structured electrode for lithium-ion batteries via 3D printing , *Materials & Design*, vol. 119, p. 417‑ 424, 2017, doi: 10.1016/j.matdes.2017.01.088.

[32] Z. Lyu *et al.*, 3D-printed electrodes for lithium metal batteries with high areal capacity and high-rate capability, *Energy Storage Materials*, vol. 24, p. 336‑ 342, 2020, doi: 10.1016/j.ensm.2019.07.041.

[33] M. Idrees, S. Ahmed, Z. Mohammed, N. S. Korivi, et V. Rangari, 3D printed supercapacitor using porous carbon derived from packaging waste, *Additive Manufacturing*, vol. 36, p. 101525, 2020, doi: 10.1016/j.addma.2020.101525.

[34] X. Li, H. Li, X. Fan, X. Shi, et J. Liang, 3D-Printed Stretchable Micro-Supercapacitor with Remarkable Areal Performance, *Advanced Energy Materials*, vol. 10, n° 14, p. 1903794, 2020, doi: 10.1002/aenm.201903794.[35] Z. Wang *et al.*, Three-Dimensional Printing of Polyaniline/Reduced Graphene Oxide Composite for High-Performance Planar Supercapacitor, *ACS Appl. Mater. Interfaces*, vol. 10, n° 12, p. 10437- 10444, 2018, doi: 10.1021/acsami.7b19635.

[35] Z. Wang *et al.*, « Three-Dimensional Printing of Polyaniline/Reduced Graphene Oxide Composite for High-Performance Planar Supercapacitor », *ACS Appl. Mater. Interfaces*, vol. 10, n° 12, p. 10437- 10444, 2018, doi: 10.1021/acsami.7b19635.

[36] S. Nesaei *et al.*, Micro additive manufacturing of glucose biosensors: A feasibility study, *Analytica Chimica Acta*, vol. 1043, p. 142- 149, 2018, doi: 10.1016/j.aca.2018.09.012.

[37] G. Postiglione, G. Natale, G. Griffini, M. Levi, et S. Turri, Conductive 3D microstructures by direct 3D printing of polymer/carbon nanotube nanocomposites via liquid deposition modeling, *Composites Part A: Applied Science and Manufacturing*, vol. 76, p. 110- 114, 2015, doi: 10.1016/j.compositesa.2015.05.014.

[38] B. Yao *et al.*, Efficient 3D Printed Pseudocapacitive Electrodes with Ultrahigh $MnO_2$ Loading, *Joule*, vol. 3, n° 2, p. 459- 470, 2019, doi: 10.1016/j.joule.2018.09.020.

[39] C. Sun, S. Liu, X. Shi, C. Lai, J. Liang, et Y. Chen, 3D printing nanocomposite gel-based thick electrode enabling both high areal capacity and rate performance for lithium-ion battery, *Chemical Engineering Journal*, vol. 381, p. 122641, 2020, doi: 10.1016/j.cej.2019.122641.

[40] J. Wang *et al.*, Toward High Areal Energy and Power Density Electrode for Li-Ion Batteries via Optimized 3D Printing Approach, *ACS Appl. Mater. Interfaces*, vol. 10, n° 46, p. 39794- 39801, 2018, doi: 10.1021/acsami.8b14797.

[41] Meyer, V., Tapin-Lingua, S., Da Silva Perez, D., Arndt, T., Kautto, J., 2012. Technical opportunities and economic challenges to produce nanofibrillated cellulos in pilot scale: NFC delivery for applications in demonstrations trials. In: Proceed. SUNPAP EU Project—Final Conference, 19–20 June, 2012, Milan, Italy. https://cordis.europa.eu/project/id/228802/reporting

[42] M. Ghodhbane, G. Menassol, D. Beneventi, D. Chaussy, L. Dubois, A. Zebda, M.N. Belgacem, Flexible doctor blade-coated abiotic cathodes for implantable glucose/oxygen biofuel cells, RSC Advances, 13, 3877–3889, 2023, doi: 10.1039/d2ra03471a.

[43] X. Li, H. Wang, J. T. Robinson, H. Sanchez, G. Diankov, H. Dai, Simultaneous Nitrogen Doping and Reduction of Graphene Oxide, *Journal of the American Chemical Society* 131 (43), 15939-15944, 2009, doi: 10.1021/ja907098f.

[44] Penven, G., Menassol, G., Alcaraz, J. P., Boucher, F., Thélu, J., El Ichi, S., ... & Martin, D. K. The biocompatibility of biofuel cells operating inside the body. Biochemical Society Transactions, 48(3), 867-879, 2020.

[45] S. Ferri, K. Kojima, et K. Sode, Review of glucose oxidases and glucose dehydrogenases: a bird's eye view of glucose sensing enzymes, *J Diabetes Sci Technol*, vol. 5, n° 5, p. 1068- 1076, 2011, doi: 10.1177/193229681100500507.

[46] S. El Ichi, A. Zebda, J.-P. Alcaraz, F. Boucher, Biocompatible implantable biofuel cell, in *2014 IEEE Conference on Biomedical Engineering and Sciences (IECBES)*, 2014, p. 51- 55. doi: 10.1109/IECBES.2014.7047553.

[47] N. Roussel, Rheological requirements for printable concretes, Cement and Concrete Research vol. 112, 76-85, 2008, doi.org/10.1016/j.cemconres.2018.04.005.

[48] C. Moser, G. Henriksson, M. E. Lindström, Specific surface area increase during cellulose nanofiber manufacturing related to energy input, *BioResources,* 11(3), 7124-7132, 2016, doi: 10.15376/biores.11.3.7124-7132

[49] W. Luo, Z. Bai, Y. Zhu, Fast removal of Co(II ) from aqueous solution using porous carboxymethyl chitosan beads and its adsorption mechanism, R*SC Advances*, 8, 13370-13387, 2018, doi:10.1039/C7RA13064C.

[50] O. Santiago, E. Navarro, M. A. Raso, T. J. Leo, Review of implantable and external abiotically catalysed glucose fuel cells and the differences between their membranes and catalysts, Applied Energy, vol. 179, 497-522, 2016, doi.org/10.1016/j.apenergy.2016.06.136.